Fabrication and STEM/EELS measurements of nanometer-scale silicon tips and filaments

B. W. Reed and J. M. Chen
School of Applied and Engineering Physics and the Cornell Nanofabrication Facility, Cornell University, Ithaca, New York 14853

N. C. MacDonald
School of Electrical Engineering and the Cornell Nanofabrication Facility, Cornell University, Ithaca, New York 14853

J. Silcox
School of Applied and Engineering Physics, Cornell University, Ithaca, New York 14853

G. F. Bertsch
Institute of Nuclear Theory, and Department of Physics, Box 351560, University of Washington, Seattle, Washington 98195
(Received 21 December 1998)

We present a series of scanning transmission electron microscopy and electron energy-loss spectroscopy (EELS) measurements of nanometer-scale single-crystal silicon tips and filaments. The tips and filaments are of a type that we are currently integrating into microelectromechanical systems. The EELS measurements reveal a number of nanometer-scale effects, some of which have already been reported in the literature for other systems. These effects include apparent upward shifts in the energies, widths, and interaction cross sections of the plasmons. In addition, we report a sharp peak at 5 eV, which we are identifying as an interband transition in the silicon. We provide theoretical explanations of the characteristics of this new peak, including an explanation of its failure to appear at any but the smallest sample diameters. Finally, we extend the theory already present in the literature with a finite-element model of EELS for nonpenetrating electrons in an arbitrary geometry. [S0163-1829(99)10131-0]

I. INTRODUCTION

In recent years, advances in microscopy and sample fabrication technology have allowed researchers to study nanometer-scale solids as never before. Many studies have focused in particular on transmission electron microscopy and electron energy-loss spectroscopy (EELS). These studies, both theoretical (Refs. 1–5, for example) and experimental,[6–13] have enhanced our understanding of the dominant physics at nanometer scales. As microscale technology gradually gives way to nanoscale technology, such work becomes relevant from an engineering as well as a scientific standpoint—for one cannot design a system with nanometer-scale components without first understanding how those components will behave.

To this end, we present a series of scanning transmission electron microscopy (STEM) and EELS measurements of single-crystal silicon tips and filaments (with diameters down to 3.5 and 20 nm, respectively). To make the measurements, we developed a method of integrating these silicon structures into an open-substrate geometry suitable for STEM. We used these samples for basic measurements of the size, shape, crystal structure, and surface films of the tips, then proceeded to a detailed study of the low-energy EELS spectra of the tips. The EELS study constitutes the bulk of the present paper. We include both theoretical and experimental discussions of a number of phenomena that occur for very small sample diameters. These phenomena include a 5-eV peak associated with a silicon interband transition, an upward shift in plasmon widths and energies, and an apparent increase in EELS interaction cross sections.

This work is related to our work in microelectromechanical systems (MEMS). Our sample fabrication technique is an adaptation of a process originally designed for integrating nanometer-scale components into micrometer-scale mechanical systems. The MEMS process itself has been successfully implemented and we plan to present it in future. Since the nanoscale structures in the STEM samples are identical to those in our micromechanical devices, our STEM characterizations may have application to MEMS diagnostics.

Figure 1 illustrates the sorts of nanoscale structures we are considering. A tip [Figs. 1(a) and 1(b)] consists of a cylindrical shank, narrowing down in a cone to a roughly hemispherical end. The shank diameter is 100 to 200 nm, the final diameter of the tip is typically 3 to 4 nm, and the cone half angle is of order 10° or less. These parameters can be controlled with proper design of the photolithographic mask that produces the tips. A filament [Fig. 1(c)] is a fixed-fixed beam of uniform, roughly circular, cross section. A filament's diameter can be anything from 200 down to about 20 nm, again depending on the photolithography, and its length can range from a few micrometers to hundreds of micrometers. Everything in these images is made of single-crystal silicon.

II. SAMPLE FABRICATION AND BASIC CHARACTERIZATION

When we began this study, we were faced with the challenge of integrating the tips and filaments into a sample that could be used in the STEM system available to us. To fit into

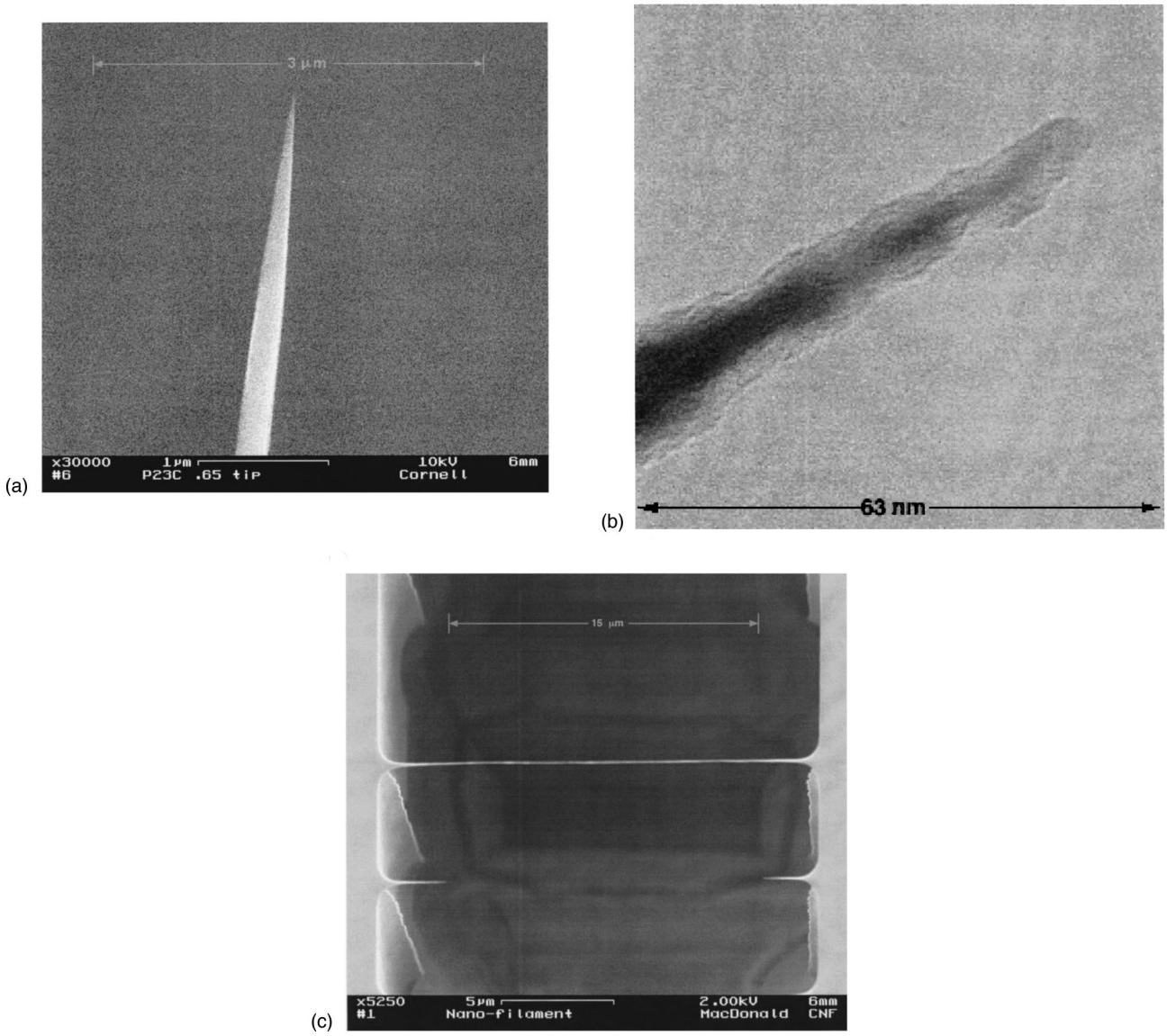

FIG. 1. Scanning electron microscopy (SEM) (a), (c) and STEM (b) images of nanometer-scale silicon structures. (a) A tip, shaped like a cylinder topped with a narrow cone. (b) Closeup of a tip. The very end looks like a hemisphere of diameter 3.5 nm. (c) A fixed-fixed filament. These filaments can have diameters ranging from 20 to 200 nm. Everything in these images is made of single-crystal silicon.

the STEM, the sample had to be roughly 1 mm on a side, and it had to be much thinner than the 400-μm-thick silicon wafers we use in our processing. Also, we needed to have holes cut entirely through the sample to allow the electron beam to pass through.

Figure 2 shows the geometry that we used to solve this problem. A square membrane 1 mm on a side and roughly 50 μm thick is separated from the 400-μm-thick portions of the wafer by eight narrow bridges of silicon. The membranes are made by etching the back side of the wafer in a high-speed fluorine-based reactive ion etcher (a Plasma Therm SLR-770 available at the Cornell Nanofabrication Facility). The center portion of the square membrane has many holes passing completely through it. Extending over and across these holes are the nanostructures—lateral silicon tips and filaments of varying sizes and shapes. Figure 2(b) is a closeup of an array of these structures. When it comes time to prepare the sample for insertion into the STEM, the eight bridges are burned away using a laser scriber at Cornell's Advanced Electronic Packaging Facility. This frees the membrane from the substrate. The membrane is then carefully picked up with tweezers and glued to a small copper washer with a 400–600-μm hole in the center, aligning the set of holes in the membrane to the hole in the washer. The combined membrane and washer are then of the right size and shape for mounting in the STEM.

The nanostructures themselves are made by thermally oxidizing released silicon beams with varying widths and heights of roughly 0.5–1.0 μm. These beams are made with a variant of the single-crystal reactive etching and metallization (SCREAM) process,[14] which we plan to discuss in future in the context of MEMS applications. When a silicon beam of square cross section is oxidized, the unoxidized silicon shrinks to a roughly circular cross section. Because of oxidation stress and other effects, this silicon remnant can have a repeatable nanometer-scale diameter even if the original structure was hundreds of nanometers across.[15,16] Thus we can reliably produce nm-scale silicon structures without

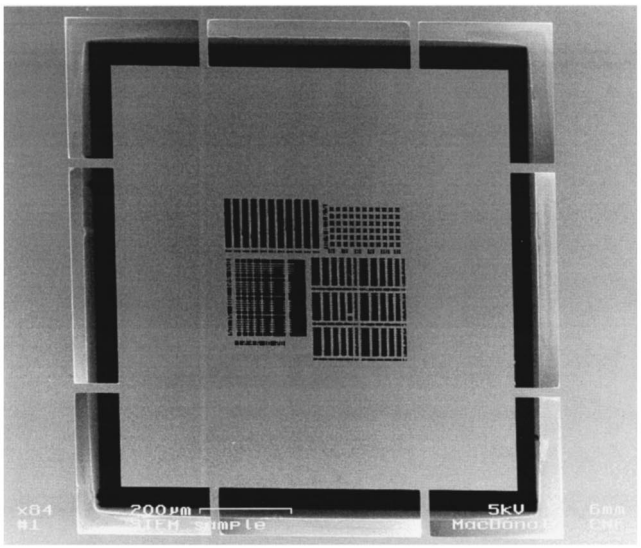

(a)

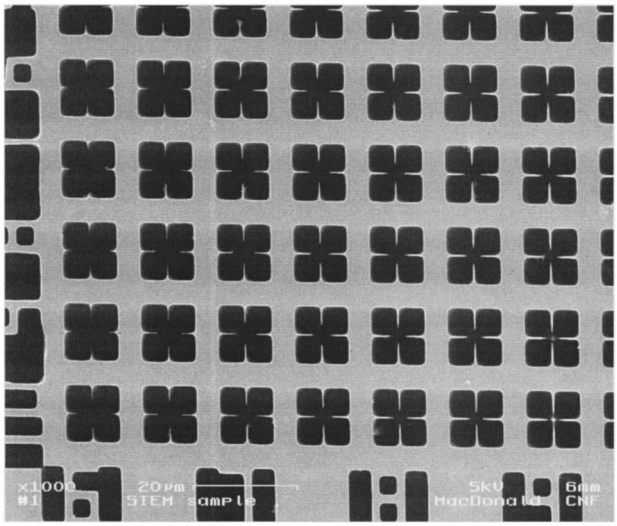

(b)

FIG. 2. SEM images of one of our STEM samples before its removal from the silicon wafer. (a) Wide view, showing the 1 mm×1 mm×50 μm membrane with eight bridges of silicon holding it in place. (b) Closeup view, showing an array of test structures, in this case sets of four tips formed in close proximity to each other.

resorting to ultrahigh-resolution patterning techniques such as electron-beam lithography. The only tools we need are photolithography, thermal oxidation, ordinary plasma processing, and hydrofluoric acid to strip the oxide, leaving the silicon structures.

We should point out that each nanostructure we look at is tailor-made. This is in contrast to another common method of studying nanometer-scale structures in transmission electron microscopy (TEM), involving the spread of large numbers of structures on a thin porous substrate (see Refs. 8 and 9 for examples). By chance, some of the nanostructures will land in a suitable orientation for viewing, with little or none of the porous substrate in the path of the electron beam. In our case, each tip and filament is specifically created with certain parameters using a photolithographic mask. We can easily produce large numbers of nominally identical structures. Also, simply by designing the holes to be sufficiently wide, we can guarantee that the membrane that supports the nanostructures is far from the path of the electron beam.

We performed the STEM measurements in a VGHB 501A STEM. Before placing the samples into the ultrahigh-vacuum (UHV) chamber, we cleaned them for 20 s in a 10:1 ethanol/HF mixture, followed by three 20-s rinses in ethanol. After the rinse, the samples were in air for less than 10 min before entering the UHV load lock, to minimize the native oxide growth on the silicon surface. EELS scans near the known absorption edges of carbon, nitrogen, and oxygen showed little or no signal, indicating that our attempts to avoid contamination were largely successful. The surface-to-bulk signal ratio in our samples, especially at the ends of the tips, should be very high, so that any surface film should be quite easy to see.

We also checked for surface contamination in a scanning Auger microscope, and determined that the contamination is determined by the chemicals used to strip the oxide and rinse the samples. If the HF solution is buffered with ammonium hydroxide, we found that a nitrogen-containing film appears on the surface, so we avoided this with the STEM samples. The ethanol/HF mixture turned out to produce the least contamination. All of the low-energy EELS spectra presented below were taken at positions where the surface was very free of contamination.

Using both microdiffraction (with a spot size of 0.2 nm) and selected area diffraction we determined that, to the limit of our ability to measure, our samples continued to be single-crystal silicon regardless of the stresses and high temperatures that occurred during their fabrication. We saw no evidence of crystal damage or surface crystallographic effects, even at the very ends of the tips or in the centers of long filaments. We refer to previous work[18] on a similar system showing oxidation-stress-induced dislocations that healed once the stress was removed. Any such crystal damage in our samples was invisible once the oxide was stripped.

Electron-beam-induced damage to our samples also did not seem to be an issue. We found that we could bombard our tips with a focused spot of 100-keV electrons for many minutes with little or no apparent change in the sample.

III. LOW-ENERGY EELS MEASUREMENT TECHNIQUES

The EELS measurements were performed with a 100-keV electron beam, an incident aperture of 10 mrad, and a collector aperture of 3.7 mrad for serial measurements and 16 mrad for parallel measurements (described below). The theory discussed in Sec. V predicts that essentially all of the low-energy EELS electrons will be scattered into angles of less than 1 mrad. Under these conditions, the electron beam can be taken to be essentially classical rather than quantum mechanical.[3,4] The spot size was typically of order 0.2 nm (see Muller and Silcox[11] and references therein for a discussion of the resolution limits in STEM EELS).

The EELS system we used has two different types of detectors—a photomultiplier tube with a scanning energy range selector, and an energy analyzer combined with a scintillator crystal and a charge-coupled device (CCD). The former measures only one energy at a time, while the latter

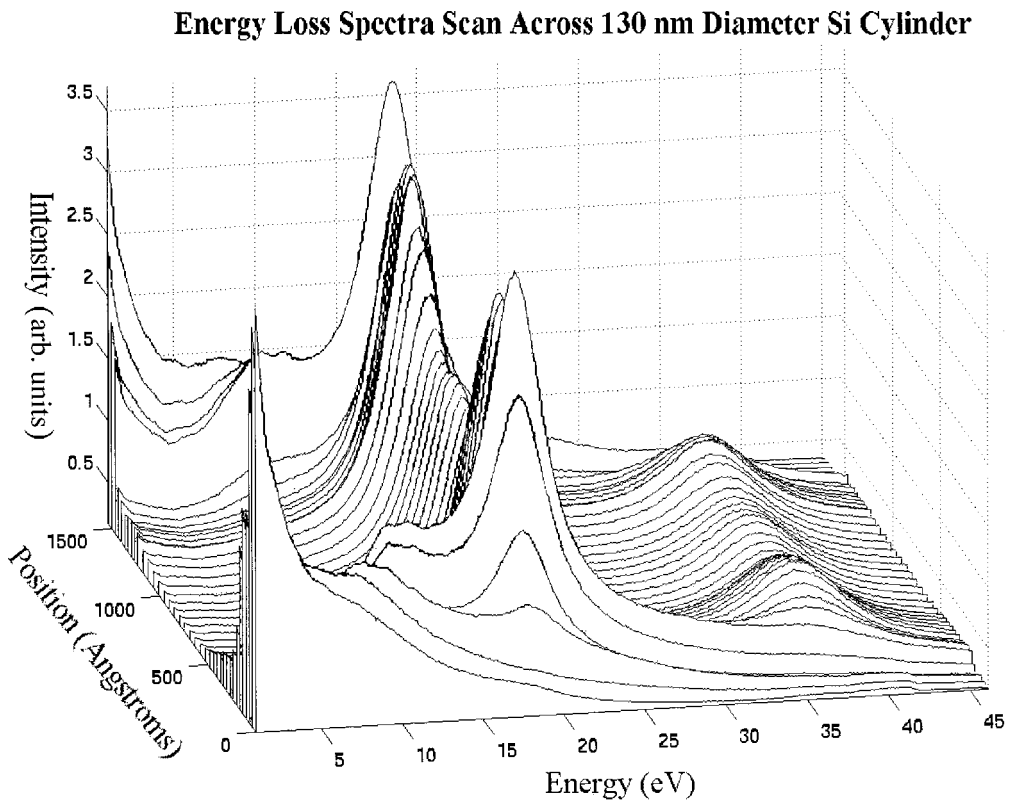

FIG. 3. Parallel EELS scan of a silicon cylinder with a diameter of roughly 130 nm. Surface, bulk, and double bulk plasmon losses are clearly visible.

collects data for all energies simultaneously. Since the signal levels for the zero-loss and plasmon peaks were very high, both were used in a current integration mode rather than a single electron pulse-counting mode. The serial detection system integrated the current indirectly using a voltage-to-frequency converter connected to a pulse counter. This introduced nonlinearities for extremely low count rates, but otherwise did not seem to significantly alter the results. Unfortunately, the constant of proportionality between the measured serial count rate and the actual number of electrons counted is unknown, as this constant varies considerably with small adjustments of the photomultiplier. Therefore, we were not able to accurately estimate counting statistics for the serial measurements.

The parallel detector had the advantages of speed and greater programmability. However, its dynamic range was barely adequate to measure the zero-loss peaks and plasmon peaks simultaneously. We found that, in order to consistently subtract off the zero-loss peak background in a way that we felt was justifiable, we had to measure the zero-loss peak with each spectrum. Therefore, our more detailed data analysis was reserved for the serial measurements, as the serial detector had more than enough dynamic range for our needs.

The parallel detector was still very useful. Any phenomenon which did not appear in both detectors was suspect. Also, when in parallel mode, it was possible to program the STEM system to step through a sequence of positions along a line, taking an EELS spectrum at each point. This gave us a quick way to find out what sorts of energy-loss modes occur in various positions on the sample. Figure 3 gives an example of this sort of measurement. This graph shows a series of parallel EELS measurements taken across the diameter of a silicon filament with a diameter of roughly 130 nm. The plot looks quite like one would expect. Starting just outside the sample, a surface plasmon at 11 eV can be excited before the beam is intersecting the actual filament (the energy appears to be lower than this at large impact parameters, which may be a retardation effect[12]). This plasmon has a peak intensity right at the edge, and at this point we also see the beginnings of the bulk plasmon at 17 eV. Further inside, the surface plasmon drops off while the bulk plasmon builds up to a maximum and the zero-loss peak drops in intensity. Eventually, multiple interactions dominate and we see the double bulk plasmon loss at 33 eV grow at the expense of the single plasmon loss. Yet further inside, the double plasmon peak loses some strength, presumably to higher order interactions. This trend continues into the center of the sample, and the entire pattern is symmetrically reversed as we pass the midpoint of the filament. When we scanned near the extreme tip, we found a narrow peak at 5 eV, which appeared nowhere else in our sample. This peak is described and theoretically explained as a surface interband transition mode in the following sections. These are the only significant low-energy peaks we encountered.

For a quick, qualitative look at the positional dependence of various energy-loss modes, this type of positional scanning is invaluable (see Ref. 8 for another example of the use of this technique). For more detailed analyses of the spectra, however, we found that the greater dynamic range of the serial detector was essential.

IV. LOW-ENERGY EELS DATA ANALYSIS TECHNIQUES

In order to clearly see the low-energy EELS peaks (especially the 5-eV peak), it was necessary to develop a consis-

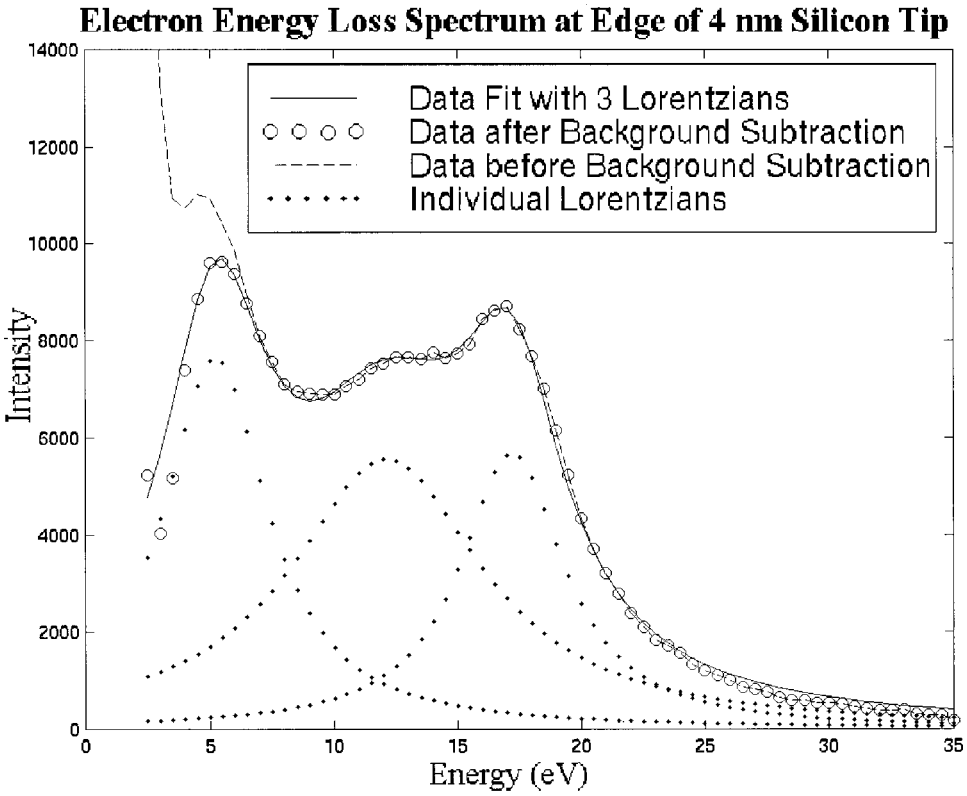

FIG. 4. A serial EELS measurement taken at the center of the tip, before and after background subtraction. Also shown is a sum-of-Lorentzians curve fit and the three individual peaks that went into the curve fit.

tent way to subtract off the background spectrum created by the tails of the zero-loss peak. The zero-loss peak did not fit sufficiently well to a Gaussian, Lorentzian, or any other simple function we tried. Instead, we fit the zero-loss peak directly to the measured spectrum of the incident beam in vacuum. The measured incident beam shape was translated and linearly scaled in both the energy and intensity axes until it optimally fit the measured zero-loss peak. A cubic spline was used for interpolation, thus turning the discrete points of the incident beam measurement into a smooth curve. The energy scale and shift parameters allowed us to compensate for random shifts in the position and width of the incident beam. The intensity scaling parameter represented a combination of the intensity fluctuation in the incident beam, the fluctuation in the photomultiplier gain, and the fraction of electrons that were scattered by the sample. The intensity shift allowed us to compensate for small changes in the detector dark current. In practice, the intensity shift parameter was unimportant and the quality of the fit was essentially as good without the parameter as with it.

Once these four fit parameters were known, we could simply subtract the scaled, shifted incident beam shape from our measured spectrum, leaving only the energy-loss spectrum. We had to ensure that this procedure cleanly removed the zero-loss peak without introducing any artifacts. To this end, we measured multiple vacuum zero-loss peaks in rapid succession and fit them to each other, one pair at a time. After fitting, the difference between two peaks tended to be significant only for energies less than roughly 3 to 4 eV. Above this energy, the residuals were consistently much lower than the typical magnitudes of the energy-loss peaks. Figure 4 shows (among other things) a measured spectrum before and after background subtraction.

The uncertainty for the serial measurements appears to be dominated by a random energy shift from point to point of order 0.05 eV. This magnitude is roughly consistent with incident beam energy shifts observed by other means. We also found that if two zero-loss peaks are measured in significantly different conditions or are separated in time by more than roughly 20 min, the residuals are far too large to be explained simply by point-to-point energy fluctuations. Therefore we had to ensure that, for every spectrum we measured, we had a recent measure of the zero-loss peak taken under identical conditions.

Once we had removed the background from the spectra, we could analyze the energy-loss spectra themselves. Since the peaks in these spectra overlapped and some of the peaks were somewhat obscured by the tails of nearby higher peaks, we fit the spectra to a sum of peaks. After trying a number of different functional forms for the shape of the peaks, we settled on Lorentzians, which consistently produced the best fits to the data. Figure 4, a plot of a typical spectrum found at the end of a tip, demonstrates this. The sum of three Lorentzians fits the curve remarkably well. We found that, within roughly one half-width at half maximum (HWHM) of the peak of a Lorentzian, the residuals of the fit appeared to be essentially random, while further out in the tails a relatively weak pattern emerged. Thus the Lorentzian function describes the main part of the response quite well. Figure 4 also shows the individual Lorentzians that make up the fit curve. We can easily identify a silicon bulk plasmon at about 17 eV, the surface plasmon at about 11 eV, and an interband transition at 5 eV. The spectrum could hardly be described with fewer than three peaks, while the Lorentzian curve fit does not suggest the need for any more. The measured plas-

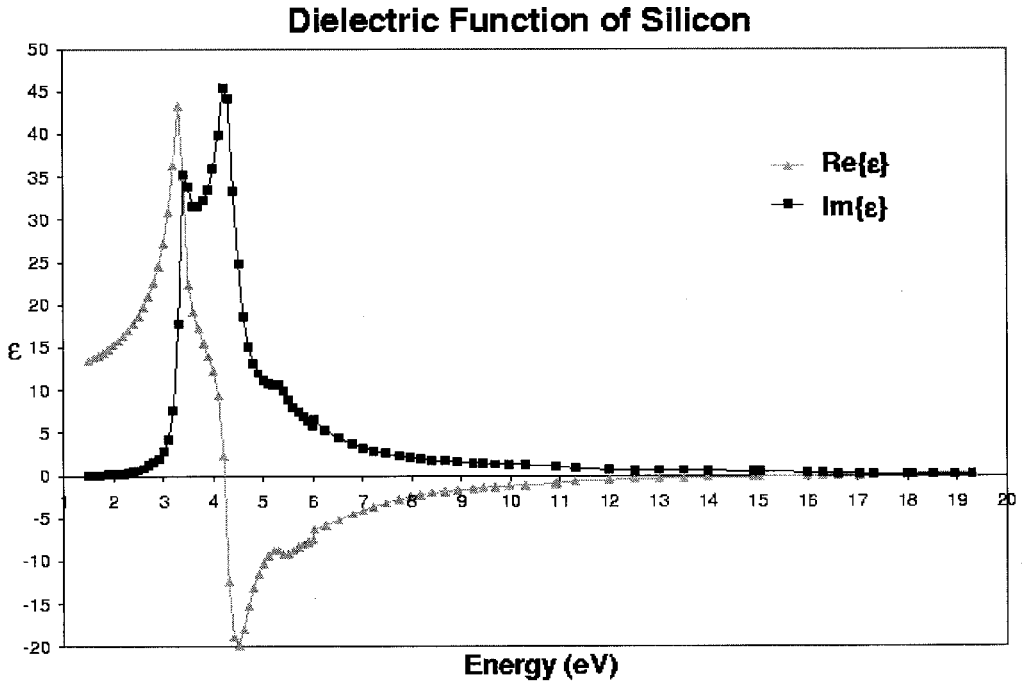

FIG. 5. Dielectric function of silicon from Refs. 20–22.

mon energies are a bit higher than expected; we will discuss this below.

We should note that we chose not to deconvolve the measured spectra with the measured shape of the zero-loss peak. We were concerned that this would introduce numerical artifacts, due to the difficulties inherent in deconvolution. Note that Moreau *et al.*[12] attempted to deconvolve their spectra in this manner, and found that in order to smooth out the artifacts they had to convolve the result with a Gaussian almost as wide as the incident beam. We chose another path—to analyze the spectra as we measured them, understanding that some fractions of the measured linewidths were due to the width of the incident beam. Since the incident beam was significantly narrower than any of our measured peaks, the error involved in this procedure should not be very large. When we wanted to compare our measured spectra with theoretical spectra, we convolved the measured incident beam with the theoretical curves.

Recognizing that our estimates of the uncertainty in each data point were very rough, we judged the quality of our curve fits both on the basis of the absolute values of the residuals and on the normalized residuals (the residuals divided by the estimated uncertainty of each data point). The uncertainty in the serial measurements was, as stated above, apparently due to a combination of counting statistics and a point-to-point energy drift of order 0.05 eV. The multiplicative factor on the counting statistics could only be roughly estimated. We judged our fits to be good when a plot of the residuals had a random appearance and rarely ventured more than a few (estimated) standard deviations from the energy axis.

To determine the robustness of our fit parameters, we studied how much they varied when we changed our fit procedure. We varied the initial guesses of the parameters, our methods of estimating data point uncertainties, and the energy ranges of data that were included in the fits. We tried deliberately misplacing the position of one peak and seeing the effect on the fit parameters of neighboring peaks. We determined how much variation in each fit parameter would turn a ''good'' fit (in the sense of the preceding paragraph) into a fit that no longer fit our criteria. The inadequacies in our data point uncertainty estimates and the poor fitting in the far tails of the Lorentzians prevented us from applying precise statistical techniques such as those found in Ref. 19.

Using these techniques, we determined that the calculated height of a dominant peak could vary by ~1–3%, while its width and energy tended to vary by ~0.1–0.2 eV. A much smaller peak in the tails of a dominant peak could have up to ten times this uncertainty, depending on the relative size of its signal. In extreme cases we concluded that we could not be sure that the smaller peak was really there at all (looking ahead to Fig. 7, the minor peaks for the 14-nm diameter are examples of this). For the 5-eV peaks, an additional uncertainty comes from imperfect removal of the nearby zero-loss peak. At most three Lorentzians could be used in the fit curve. If we tried to add a fourth peak, we found that the parameters of the weakest peak were essentially meaningless because of the coupling of parameters among the peaks. This would seem to be an inherent problem with fitting multiple peaks, each with a HWHM of several eV and fairly broad tails, into an energy range of 15–25 eV.

V. EELS RESULTS

To interpret our low-energy EELS spectra, we begin with a description of the complex dielectric function of silicon, which is plotted in Fig. 5. These data were calculated from optical measurements found in Refs. 20–22. The applicability to EELS of optically measured dielectric functions has been established in the literature.[12] For high frequencies, the dielectric function looks much like one would expect from the Drude model, while for lower frequencies the behavior is

dominated by a resonance that has been associated with interband transitions.[23] The transition between the two regions occurs at roughly 5 to 6 eV. This frequency-dependent dielectric function was the only material property used in our theoretical calculations. We neglected spatial dispersion and anisotropy, and assumed that the material properties were constant throughout the solid. Of course these approximations must break down as one approaches atomic scales, and in fact we will see some discrepancies between theory and experiment at tip extremities.

Wide portions of our samples (with diameters greater than roughly 50 nm) mostly showed expected behavior—just a steady rise and fall of surface and bulk plasmon responses such as we see in Fig. 3. The exception is a shift of the surface plasmon to lower energies for impact parameters far from the edge, both inside and outside the silicon. Some of this behavior can be seen in Fig. 3. The plasmon energy apparently drops to as low as 8–9 eV (from 11 eV) for impact parameters of order 10 nm. The same phenomenon occurs in the surface plasmons for both spherical metal particles[17] and planar interfaces.[12] The energy shift is due to relativistic effects.

We encountered some additional phenomena as the diameter of the silicon was reduced, especially at the extreme tip where the diameter was 3.5 nm. Both the energies and the widths of the surface and bulk plasmon peaks appeared to increase as the diameter was reduced (see Fig. 6). The trend is fairly strong for the surface plasmon, but we should point out that the shifts are not much larger than the uncertainties in most cases. Batson[6] has noted an increase in plasmon widths in small geometries due to increased surface scattering, but this effect can only explain part of our observed width increase. The rest of the effect may be due to spatial dispersion, a change in the surface characteristics of the material, or other nm-scale effects.[24] The onset of this effect appears to be at a diameter of a few tens of nm. The effect on the surface plasmon width is particularly strong.

Next consider Fig. 7, which shows experimental and theoretical EELS spectra for an electron beam passing within 1 nm of the silicon surface, both for a tip and for a section further back from the tip which may be approximated as a cylinder of diameter 14 nm. For the wide diameter, we applied Eq. (1) below, taken from Bertsch, Esbensen, and Reed,[5] which gives the energy-loss probability for a classical electron passing outside an infinite cylinder. For the tip, we used a finite-element calculation (which is detailed in the Appendix to this paper) and an empirically determined tip shape. In both cases the theoretical spectrum was convolved with the measured spectrum of the incident beam in such a way that the absolute count rates and the widths of the peaks should be correct (in light of the results of Ritchie and Howie[4]).

We can see that, for the 14-nm-diam cylinder, the surface plasmon peak at 11 eV has very nearly the right height and energy, but that the theoretical width is too small by a factor of roughly 1.5. Even the small rises at 5 and 15 eV appear in the measured data—though they are harder to see in the measurement due to the wider tails of the surface plasmon. Indeed, the 15-eV peak is so slight that we cannot say with certainty that it is present at all. So, for the 14-nm diameter, it would seem that our simple theory adequately captures the relevant physics, apart from additional broadening of the surface plasmon.

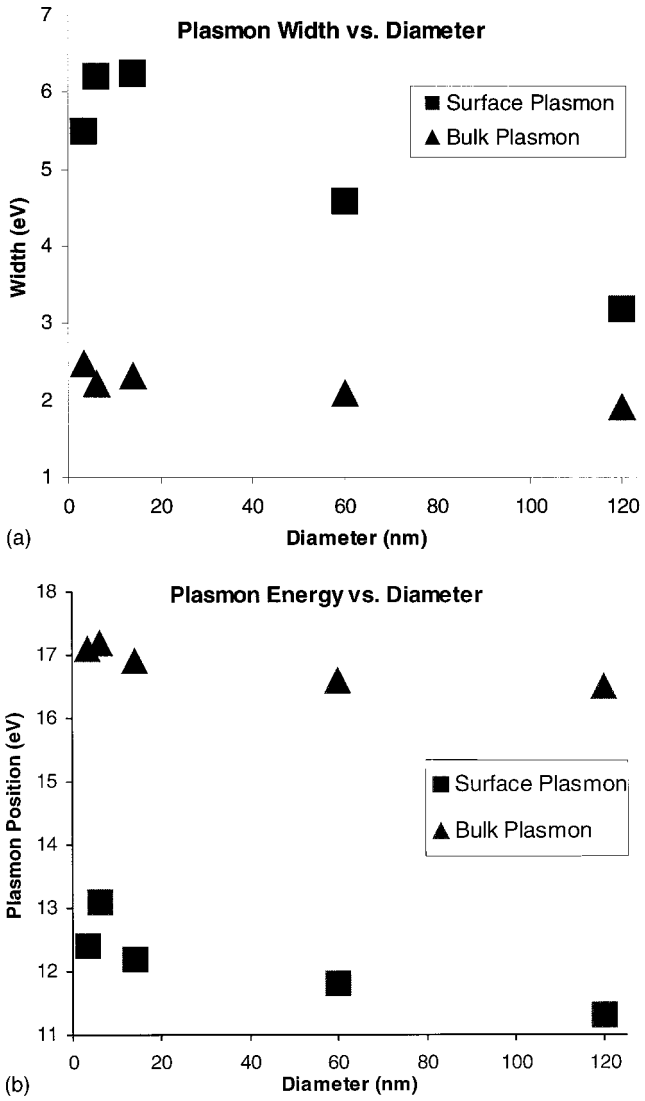

FIG. 6. The trend of (a) the widths, and (b) the peak energies of the bulk and surface plasmons at different diameters.

When we compare the results for the tip, however, we can see some major discrepancies, the most obvious of which is a shortfall in theoretical intensity by roughly a factor of 3. This suggests that the interaction cross section is somehow being enhanced through a mechanism not accounted for in our simple theory. Also, the peaks are much higher in energy for the measurement than for the theory. This indicates that both the interband transition and the surface plasmon are occurring at higher energies than they would otherwise. These energies are determined by the band structure and the electron density. Recall that the diameter at the tip is only 3.5 nm, so that a majority of the silicon atoms are within a lattice constant of the surface. It would not be surprising if the material properties at the tip were somewhat different from those of bulk silicon, due to surface effects. Batson and Heath[9] have obtained similar results for sample diameters comparable to ours. They have attributed the results to quantum effects and to shifts in the electronic band structure. We believe that we are seeing the same phenomenon. The sizes of the effects we observe are similar to the results of Batson

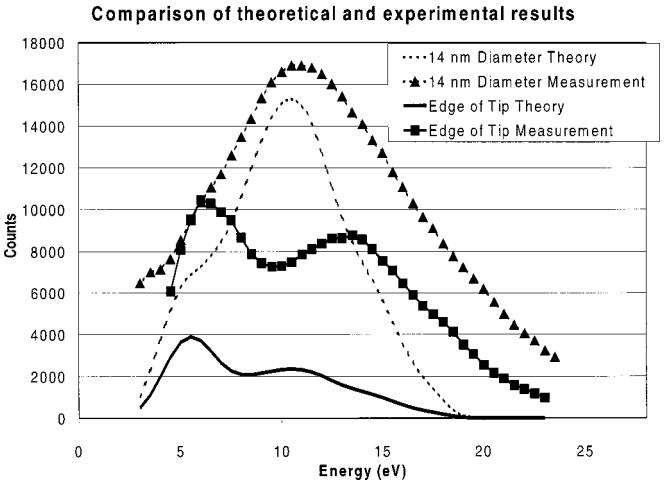

FIG. 7. Theoretical and experimental EELS spectra for a 100-keV electron beam passing just outside a 14-nm-diam cylinder and a 3.5-nm-diam tip. The theoretical curves have been convolved with a measured zero-loss peak, to allow direct comparison. The theory for the tip uses an empirically generated finite-element model of one of our tips.

and Heath for comparable diameters.

So we have seen a number of effects that apparently confirm the observations and theoretical predictions of several previous workers.

VI. THE INTERBAND TRANSITION PEAK

In addition to the phenomena described in Sec. V, we report a low-energy peak dominating the spectrum at the extreme tip, which we can see in Fig. 4. This peak is quite narrow (typical HWHM=2.4 eV), and occurs right at the upper edge of the interband transition resonance, or about 4.8–5.3 eV. This peak only appeared where the diameter of the silicon was extremely small. For the very tip (radius equal to 3.5 nm), the low-energy peak height often exceeded both plasmon peak heights. At a diameter of 6 nm, the peak was visible but not very strong. Further back from the tip, where the diameter was roughly 14 nm, the low-energy peak was almost invisible in the tails of the surface plasmon and the incident beam (Fig. 7). At still larger diameters, the peak vanished without a trace. This behavior was quite repeatable, occurring in several samples measured on different days using both serial and parallel detectors.

The height of this peak appears to be much less dependent on impact parameter than the heights of the other peaks. As we moved the incident beam from the very center of the tip to a point just outside it, the 5-eV peak lost perhaps 10% of its magnitude, the surface plasmon peak lost roughly 30%, and the bulk plasmon peak lost over 80%. This suggests that the spatial extent of the lower-energy modes is greater, which is not surprising—previous analyses of the problem (Ref. 11, and references therein) predict a spatial dependence of $\exp(-2b\omega/v)$, where b is the impact parameter, ω is the angular frequency of the energy loss, and v is the speed of the electron. Our analysis, detailed below, produces the same exponential dependence. Thus the lower the energy, the greater the range of interaction. For the 5-eV peak, $v/2\omega$ is roughly 11 nm.

Our theoretical analysis is based on a recent paper,[5] which calculates the electron energy-loss spectrum for nonpenetrating electrons passing perpendicularly to an infinite cylinder. The electrons are taken to follow a classical trajectory (see Refs. 3 and 4 for a discussion of the issues involved with this assumption). Relativistic effects are ignored. Since the cone half angles of our tips are less than 10°, approximating the local geometry as a cylinder should not introduce a large discrepancy except right at the tip, where the local geometry is more like a hemisphere at the end of a cylinder.

This theory does in fact predict a narrow, low-energy peak, appearing only at very small radii, with relatively little variation of peak height with impact parameter. The theoretical peak occurs at approximately 4.75 eV, with a typical width (HWHM) of 1.0–1.5 eV. To see where these results come from, we proceed with an analysis of the relevant equations from Ref. 5. The transition probability per unit energy is given by

$$\frac{dP}{dE}=\frac{e^2b^2}{\pi^2\hbar^2v^2}\sum_m\int_{-\infty}^{\infty}dk\,xI_m(x)I_m'(x)\mathrm{Im}\,\Pi_{mk}|F_m(\xi,kb)|^2,$$

$$x=|k|R,\quad \xi=b\omega/v. \tag{1}$$

The integrand contains a term which includes the material response,

$$\Pi_{mk}=\frac{\varepsilon-1}{1+(\varepsilon-1)xI_m'(x)K_m(x)}, \tag{2}$$

and a term that behaves like an interaction amplitude,

$$F_m(\xi,u)=\frac{\pi e^{-\sqrt{u^2+\xi^2}}}{\sqrt{u^2+\xi^2}}\left(\frac{\sqrt{u^2+\xi^2}+\xi}{|u|}\right)^m. \tag{3}$$

In these equations, b is the impact parameter relative to the center of the cylinder, R is the radius of the cylinder, $\hbar\omega$ is the electron energy loss, ε is the dielectric function of silicon, v is the speed of the passing electron, and I_m and K_m are modified Bessel functions of the first and second kinds. We will define $b'=(b-R)$ to be the impact parameter relative to the edge of the cylinder.

Note that, if k is much greater than ω/v, the integrand will be cut off exponentially as k increases. For our measurements, ω/v is of order 0.1 rad/nm. We find that unless m and ω are rather large and/or b' is very small, essentially all of the area under the curve is within the region $|k|<1.0$ rad/nm (and in fact often the range is much smaller than this, of order 0.15–0.2 rad/nm). For R of order 1–2 nm, we can (to a first approximation) take $|k|R$ to be small, which allows us to use simple approximations for the Bessel functions in the integrand. The $xI_m(x)I_m'(x)$ factor in the integrand is interesting primarily in that it contributes a radius dependence of $R^{2(m+\delta_{m0})}$.

We next consider the material response factor in this approximation:

$$\mathrm{Im}\,\Pi_{mk}\approx\begin{cases}\mathrm{Im}\,\varepsilon, & m=0\\ 2\,\mathrm{Im}\dfrac{\varepsilon-1}{\varepsilon+1}, & m\neq 0.\end{cases} \tag{4}$$

For $m=0$, this term is large only if ε has a large imaginary part. Referring back to Fig. 5, we find that this occurs only in a narrow range in the vicinity of the interband transition. For $m\neq 0$, this term is large if $\mathrm{Re}\,\varepsilon$ is close to -1 and $\mathrm{Im}\,\varepsilon$ is rather small. This occurs exclusively at the energy of the surface plasmon (-11 eV). So we find that we expect to see two completely different sorts of excitations: $m=0$ surface modes associated with an interband transition at 5 eV, and 11-eV surface plasmons for nonzero values of m. Further, because of the $R^{2(m+\delta_{m0})}$ dependence in the integrand, we can expect that the $m=0$ modes will be very difficult to see for large values of R, since the signal will be dominated by modes with larger m values (a similar effect happens in a spherical geometry, with low-l modes dominating at small diameters[13]).

To see this last point explicitly, we consider Fig. 8, which shows the R dependence of the theoretical response for various values of energy, m, and b' (calculated using a program written in MATLAB). In our measurement conditions, an EELS peak will be just barely visible somewhere in the mid-10^{-5}/eV range. In Fig. 8(a), we have taken $b'=1$ nm and chosen to look at the surface plasmon response at 11 eV. As expected, the $m=0$ mode never dominates the response, while the higher-m modes dominate at progressively higher radii (with each positive m value peaking for R roughly equal to 10 nm times m). The slope on the log-log plot at small R is approximately $1.5(m+\delta_{m,0})$, compared to the power law of $2.0(m+\delta_{m,0})$ predicted by the very rough approximations we have made.

Figure 8(b) is a similar plot for 4.5 eV, where we have also elected to show a variety of b' values. In this case, the signal is very small—almost too small to see—unless we have $m=0$ and R less than a few tens of nm. Finally we have Fig. 8(c), which shows the total response for all values of m at the two energies of interest. The interband transition peak dominates at small R and the surface plasmon at large R, with the transition occurring for R equal to b' plus a few nanometers. The interband transition peak should be very hard to see for R much greater than 10 nm. Either b' will be small, in which case this peak will be swamped by the surface plasmon peak, or b' will be large, so that the transition probability is very small, and the peak will be lost in the tails of the zero-loss peak. As we have seen in Fig. 7, this is exactly what we measured. We should point out that the experimental curves in Fig. 7 are only two of several dozen serial EELS spectra we obtained, none of which contradicted this result.

At this point we should summarize this argument in more intuitive terms. Electrodynamic analysis, assuming a cylindrical geometry, reveals that two kinds of surface modes can contribute significantly to the energy loss. The first is an azimuthally symmetric ($m=0$) mode at an energy which the material itself tends to absorb. The imaginary part of ε must be large for this mode to be significant. In a semiconductor, this will occur at the energy of a direct interband transition. The second type of mode is an azimuthally asymmetric ($m\neq 0$) excitation associated with the sudden change from a plasmalike material to a vacuum—a surface plasmon. These two types of excitations occur at different energies, but they are close enough together for the tails of one to interfere with the visibility of the other. Since larger m values tend to dominate the response at larger diameters, the $m=0$ interband peak will generally be swamped by the surface plasmon unless the diameter is quite small. This should occur not just for silicon but for any material with an $\varepsilon(\omega)$ curve qualitatively similar to that in Fig. 5, that is, essentially any semiconductor. If a material's interband resonance is at a very low energy, though, the peak may be obscured by the tails of the zero-loss peak. As we shall see below, finite-element simulations indicate that this effect is not restricted to a cylindrical geometry, and should happen whenever the electron beam passes near a region of nm-scale surface curvature.

A family of curves of varying b' tends to be evenly spaced on the logarithmic y axes of the plots in Fig. 8. For $k\ll\omega/v$, the F_m^2 factor in the integrand contributes a b dependence of $\exp(-2b\omega/v)$, and this tends to explain the spacings of these curves to within 10% or better. The approximation breaks down somewhat for the low-energy curves at very low radii, but even in this case the discrepancy in the spacing is not terribly large. So it would appear that this $\exp(-2b\omega/v)$ dependence in the integrand determines most of the dependence of peak height on impact parameter. In general, higher-energy peaks will be more sensitive to the impact parameter. For a 5-eV energy loss and a speed v consistent with a 100-keV electron, $v/2\omega$ comes out to 11 nm, so that the beam can miss the sample by several multiples of the radius and still significantly excite the interband transition.

So, to summarize the theoretical predictions, the low-energy peak should be very narrow, it should be visible only for radii of order 10 nm or less, and it should have relatively little dependence of peak height on impact parameter. This is precisely what we observed experimentally. However, the theory assumed the sample to be an infinitely long cylinder. We were concerned that some of these predictions, obtained by picking apart Eqs. (1)–(3), might be artifacts of this assumption, so we set out to develop a more general theory. In the Appendix of this paper we show how we used finite surface elements to calculate EELS for nonpenetrating electrons in an arbitrary geometry. The results obtained by this method were substantially the same as those obtained for the infinite cylinder. Using a more realistic tip shape, we found that the 5-eV peak still appears only near regions of small (<10 nm) radii, regardless of whether the nearby shape is cylindrical, hemispherical, or tiplike. This analysis also shows that the $\exp(-2b\omega/v)$ dependence is quite general (where in this case b can be taken roughly to be the closest approach of the electron beam to the sample surface). In short, the results of the finite-element calculations suggest that the characteristics of this interband transition peak are due to the nanometer scale of the material rather than to a specific geometry.

VII. SUMMARY AND FUTURE WORK

We have demonstrated a reliable technique to integrate nanometer-scale single-crystal silicon lateral tips and filaments in an open-substrate geometry, using ordinary microfabrication tools. We have also presented basic characterizations of the size, shape, crystal structure, and surface contamination of the tips and filaments. The tips can be made very sharp and very clean, allowing us to study the charac-

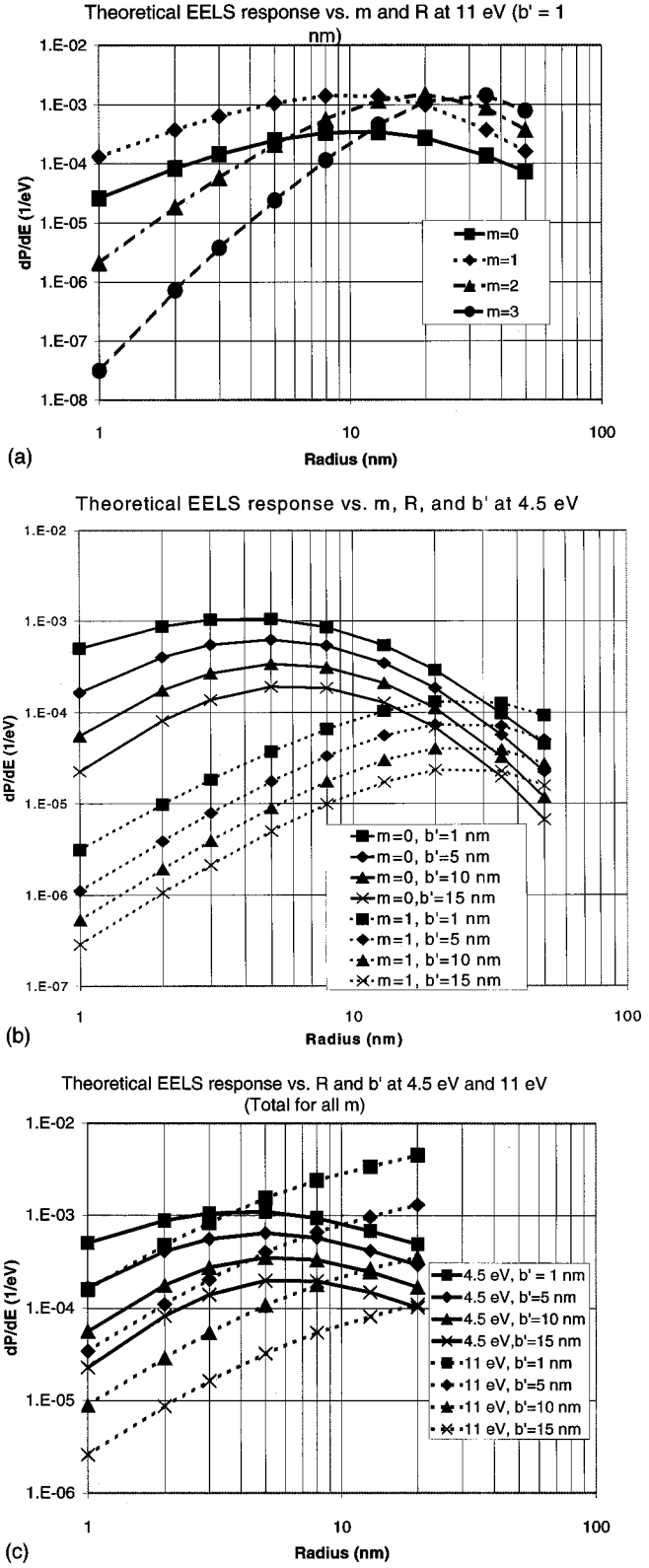

FIG. 8. Theoretical EELS response for an infinite cylinder at various values of azimuthal mode number m, angular frequency of energy loss ω, cylinder radius R, and impact parameter relative to the edge b'. (a) The surface plasmon response at varying radii for several values of m. (b) Comparison of $m=0$ and 1 responses for the interband peak. (c) Interband and surface plasmon responses at varying radii for several values of b'.

teristics of nanometer-scale silicon structures with minimal complication.

We have also performed a series of low-energy EELS measurements and found a number of phenomena, most of which have already been reported in the literature. These effects include a broadening and upward energy shift of plasmons and an increase in interaction cross section at small sample diameters, as well as a downward shift in surface plasmon energy as the electron beam moves away from the interface. At very small diameters we detected an interband transition peak which, to our knowledge, has not yet been reported in the literature. We present a detailed theoretical analysis of the characteristics of this peak and confirm these predictions with measurements. We also find that, except for certain nanometer-scale and relativistic effects, our simple theory agrees quite well with experiment.

The very same sorts of tips and filaments have been integrated into micromechanical systems, complete with electrical contact and isolation systems. We will present these results in the near future. Briefly, we are able to produce multiple-tip structures with each tip mounted on its own independent 3-degree-of-freedom actuator, and with independent electrical contact to each tip. We can also make actuators to apply tension and lateral force to our fixed-fixed filaments, while running electrical current through the filaments. We are working on ways to coat the tips and filament with ultrathin metals and silicides. The purpose of these devices is to study the mechanical characteristics and the interactions of our nanometer-scale structures.

The present paper began simply as an attempt to characterize our tips and filaments so that we could better understand the components of our micro/nanomechanical devices. However, as the reader can clearly see, our EELS results drove us into an entirely different context.

ACKNOWLEDGMENTS

We would principally like to thank Mick Thomas for operating the STEM. We would also like to thank David Muller and Earl Kirkland for helping us to analyze our data and understand the subtleties of STEM measurement. The staff of the Cornell Nanofabrication Facility and the Advanced Electronic Packaging Facility have, as always, been extremely helpful in answering questions, suggesting plans of attack, and keeping the equipment in fine operating condition. We would also like to thank our many co-workers in the MEMS community at Cornell, for exchanging ideas and sharing technical experience over the years. The UHV/STEM facility at Cornell University is funded under NSF Grant No. DMR-936 2275 through the Cornell Center for Materials Research. B.W.R. and J.M.C. were supported under DARPA Contract No. DABT63-95-C-0121.

APPENDIX: FINITE-ELEMENT MODELING OF EELS FOR NONPENETRATING ELECTRONS

In order to ensure that the theoretical results described in Sec. VI were not simply artifacts of the assumption of a cylindrical geometry, we decided to extend the theory to an arbitrary geometry, using finite surface elements. This allowed us to simulate EELS spectra for an empirically deter-

mined tip shape and compare it directly both with experimental results and with the theoretical results for the infinite cylinder (as in Fig. 7). As we will see below, our finite-element calculations are consistent with the analytic results. We have tried to keep the notation consistent with that in Ref. 5.

We start with a collection of N surface elements with areas A_j, centers $\vec{r}_j=(x_j,y_j,z_j)$, and outward-pointing unit normals $\hat{n}_j$. An electron will pass outside this surface on the trajectory $\vec{r}_e=\vec{b}+\hat{y}vt=(b_x,vt,b_z)$, producing an electric field and potential $E_{\rm ext}$ and $\Phi_{\rm ext}$. The resulting induced charge on the surface will produce an additional electric field and potential E_s and Φ_s, which will then act on the charge, slowing it down. The calculation is a straightforward application of classical electromagnetic theory. We are neglecting all relativistic effects and treating the fields in the electrostatic approximation. Unfortunately, we have not yet found a simple way to properly account for relativistic effects in this model.

From Ref. 5, the energy-loss probability per unit energy is given by

$$\frac{dP}{dE}=\frac{e}{\pi\hbar^2 v}\,\mathrm{Im}\int_{-\infty}^{\infty}dy\,\exp(-i\omega y/v)\tilde{\Phi}_s(\vec{r}_e,\omega), \quad \text{(A1)}$$

where a tilde denotes a Fourier transform with respect to time. We can calculate $\tilde{\Phi}_s$ in terms of the surface charge σ_j on each surface element with a simple application of Coulomb's law:

$$\tilde{\Phi}_s=\sum_j \frac{A_j\tilde{\sigma}_j}{|\vec{r}_e-\vec{r}_j|}. \quad \text{(A2)}$$

Upon substituting Eq. (A2) into Eq. (A1), we find that the integral can be performed analytically, yielding

$$\frac{dP}{dE}=\frac{2e}{\pi\hbar^2 v}\,\mathrm{Im}\sum_j A_j\tilde{\sigma}_j\exp(-i\omega y_j/v)K_0(\lambda_j), \quad \text{(A3)}$$

where K_0 is a modified Bessel function of the second kind and

$$\lambda_j=(\omega/v)\sqrt{(x_j-b_x)^2+(z_j-b_z)^2}. \quad \text{(A4)}$$

Equation (5) in Ref. 5 relates the normal component of the electric field immediately outside the surface to the surface charge density σ:

$$4\pi\tilde{\sigma}=\frac{\varepsilon(\omega)-1}{\varepsilon(\omega)}\hat{n}\cdot\tilde{\vec{E}}_+. \quad \text{(A5)}$$

The electric field in this equation is the total of $E_{\rm ext}$ and E_s. $\tilde{\Phi}_{\rm ext}$ is given in Ref. 5, Eq. (13), as

$$\tilde{\Phi}_{\rm ext}=\frac{-2e}{v}e^{i\omega y/v}K_0\left(\frac{\omega}{v}\sqrt{(x-b_x)^2+(z-b_z)^2}\right), \quad \text{(A6)}$$

and by taking the gradient of this at the location of surface element j we obtain

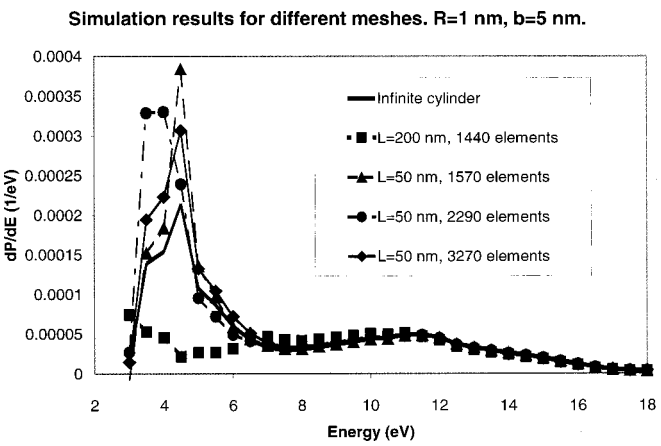

FIG. 9. The effect of the mesh density and cylinder length on the simulation results for a 2-nm-diam cylinder. The ''infinite cylinder'' result is from Eq. (1), taken from Ref. 5. The other results are from our finite-element model. The low mesh density completely fails to capture the low-energy peak.

$$\tilde{\vec{E}}_{+\mathrm{ext},j}=\frac{2e\omega}{v}\exp(i\omega y_j/v)\times\left(\frac{\omega}{v\lambda_j}(\vec{b}-\vec{r}_{\perp j})K_1(\lambda_j)+i\hat{y}K_0(\lambda_j)\right),$$

$$\vec{r}_{\perp j}=(x_j,0,z_j). \quad \text{(A7)}$$

The field due to the surface charge, according to Coulomb's law, is

$$\tilde{\vec{E}}_{+s,j}=\sum_{k\neq j}A_k\tilde{\sigma}_k\frac{\vec{r}_j-\vec{r}_k}{|\vec{r}_j-\vec{r}_k|^3}+2\pi\tilde{\sigma}_j\hat{n}_i. \quad \text{(A8)}$$

Note the self-term is simply the field due to a uniform surface charge density taken immediately outside the surface.

Combining these equations, we arrive at N equations in the N unknowns $\tilde{\sigma}_j$,

$$2\pi\frac{\varepsilon+1}{\varepsilon-1}\tilde{\sigma}_j-\sum_{k\neq j}\frac{\hat{n}_j\cdot(\vec{r}_j-\vec{r}_k)}{|\vec{r}_j-\vec{r}_k|^3}A_k\tilde{\sigma}_k=\hat{n}_j\cdot\tilde{\vec{E}}_{+\mathrm{ext},j}. \quad \text{(A9)}$$

So one must simply solve these linear equations to obtain $\tilde{\sigma}_j$ and insert the result into Eq. (A3). This is done numerically, separately for each value of ω, using a program written in MATLAB.

To verify the validity of our surface element technique, we directly compared the results given by Eq. (1) (valid for an infinite cylinder) with the results given by Eqs. (A3) and (A9) for a finite set of surface elements approximating a cylinder. Figure 9 shows the results of such a comparison. The finite-element model should, ideally, match the results for the infinite cylinder. We varied the length and the surface element density of the cylinder. The mesh density was greatest for the regions nearest the incident beam, where the surface charge density changes considerably from point to point. For energies greater than about 8 eV, the results match up quite closely in all cases. The curves begin to diverge at lower energies. The denser cylinders give much better results. There does not appear to be much need to increase the

length of the cylinder above 50 nm—it is far more effective to increase the mesh density than to increase the length of the cylinder. The long cylinder with low mesh density misses the low-energy peak completely, while the short cylinder with very high mesh density matches the low-energy shape quite well but predicts an amplitude which is somewhat too high.

With lengths greater than 50 nm and more than 2000–3000 surface elements, we find that we are entering a region of rapidly diminishing returns. Note that, if we have N surface elements, our computer must set up and solve an $N \times N$ complex matrix equation for each energy. We run into practical difficulties in terms of both time and computer memory when N exceeds roughly 3000. We conclude that, with a well-designed mesh, we can get quantitatively reliable results down to about 4 eV, provided that we scale down the amplitude somewhat for energies below 6 eV.

For large λ_j, the K Bessel functions in Eqs. (A3) and (A9) give roughly an $\exp(-2\lambda_j)$ factor for the contribution of surface element j to the energy-loss probability. This is directly analogous to the $\exp(-2\omega b/v)$ factor that comes up in Sec. VI, where in this case the impact parameter b is replaced by the closest approach of the electron beam to the surface element in question. As we have pointed out earlier, for $\hbar\omega = 5$ eV and v consistent with a 100-keV electron, we find that $v/2\omega$ is 11 nm. To get good results at this energy, it is not surprising to find that we need to include all surface elements within roughly 20–30 nm of the incident beam. And this also gives us some explanation of why a mesh that works well at high energy suddenly becomes inadequate at lower energy, as surface elements further and further from the incident beam start to contribute significantly to the energy loss.

When we simulate EELS for an empirically determined tip shape (with a final radius just under 2 nm), we find that the 5-eV peak is dominant only when the electron beam passes very close to the tip, confirming our experimental results. If we increase the tip radius, the 5-eV peak becomes less and less dominant, and starts to be lost in the tails of the surface plasmon peak at a radius of roughly 10 nm. This is essentially the same result we obtained for an infinite circular cylinder. This suggests that the exact extended shape of the specimen is less important than the surface curvature near the incident beam (where ''near'' means within a few multiples of $v/2\omega$). In other words, the interband transition peak appears to be more of a general nanometer-scale phenomenon than an accident of our particular geometry.

[1] A. Rivacoba, N. Zabala, and P. M. Echenique, Phys. Rev. Lett. **69**, 3362 (1992).
[2] A. Rivacoba, P. Apell, and N. Zabala, Nucl. Instrum. Methods Phys. Res. B **96**, 465 (1995).
[3] R. H. Ritchie, Philos. Mag. A **44**, 931 (1981).
[4] R. H. Ritchie and A. Howie, Philos. Mag. A **58**, 753 (1988).
[5] G. F. Bertsch, H. Esbensen, and B. W. Reed, Phys. Rev. B **58**, 14 031 (1998).
[6] P. E. Batson, Solid State Commun. **34**, 477 (1980).
[7] R. Vincent and J. Silcox, Phys. Rev. Lett. **31**, 1487 (1973).
[8] H. Cohen, T. Maniv, R. Tenne, Y. Rosenfeld Hacohen, O. Stephan, and C. Colliex, Phys. Rev. Lett. **80**, 782 (1998).
[9] P. E. Batson and J. R. Heath, Phys. Rev. Lett. **71**, 911 (1993).
[10] R. Kuzuo, M. Terauchi, and M. Tanaka, Jpn. J. Appl. Phys., Part 2 **31**, L1484 (1992).
[11] D. A. Muller and J. Silcox, Ultramicroscopy **59**, 195 (1995).
[12] P. Moreau, N. Brun, C. A. Walsh, C. Colliex, and A. Howie, Phys. Rev. B **56**, 6774 (1997).
[13] H. Petersen, Solid State Commun. **23**, 931 (1977).
[14] N. C. MacDonald, Microelectron. Eng. **32**, 49 (1996).
[15] R. B. Marcus and T. T. Sheng, J. Electrochem. Soc. **129**, 1278 (1982).
[16] T. S. Ravi, R. B. Marcus, and D. Liu, J. Vac. Sci. Technol. B **9**, 2733 (1991).
[17] C. Bohren and D. Huffman, *Absorption and Scattering of Light by Small Particles* (Wiley, New York, 1983), Fig. 12.3.
[18] N. D. Theodore, S. C. Arney, C. B. Carter, and N. C. MacDonald, J. Electrochem. Soc. **139**, 290 (1992).
[19] P. R. Bevington, *Data Reduction and Error Analysis for the Physical Sciences* (McGraw-Hill, New York, 1969), pp. 187–246.
[20] D. E. Aspnes and A. A. Studna, Phys. Rev. B **27**, 985 (1983).
[21] T. Sasaki and K. Ishiguro, Phys. Rev. **127**, 1091 (1962).
[22] H. R. Phillipp and E. A. Taft, Phys. Rev. **120**, 37 (1960).
[23] H. Ehrenreich, H. R. Philipp, and J. C. Phillips, Phys. Rev. Lett. **8**, 59 (1962).
[24] G. C. Aers, A. D. Boardman, and B. V. Paranjape, J. Phys. F **10**, 53 (1980).